PNAS RESEARCH ARTICLE | ENGINEERING

Artificial neuromorphic cognitive skins based on distributed biaxially stretchable elastomeric synaptic transistors

Hyunseok Shim[a,b], Seonmin Jang[a,b], Anish Thukral[c], Seongsik Jeong[d], Hyeseon Jo[d], Bin Kan[c], Shubham Patel[a,c], Guodan Wei[e], Wei Lan[f], Hae-Jin Kim[d,1], and Cunjiang Yu[a,b,c,g,h,i,1]

Edited by John Rogers, Northwestern University, Evanston, IL; received March 25, 2022; accepted April 29, 2022

Cephalopod (e.g., squid, octopus, etc.) skin is a soft cognitive organ capable of elastic deformation, visualizing, stealth, and camouflaging through complex biological processes of sensing, recognition, neurologic processing, and actuation in a noncentralized, distributed manner. However, none of the existing artificial skin devices have shown distributed neuromorphic processing and cognition capabilities similar to those of a cephalopod skin. Thus, the creation of an elastic, biaxially stretchy device with embedded, distributed neurologic and cognitive functions mimicking a cephalopod skin can play a pivotal role in emerging robotics, wearables, skin prosthetics, bioelectronics, etc. This paper introduces artificial neuromorphic cognitive skins based on arrayed, biaxially stretchable synaptic transistors constructed entirely out of elastomeric materials. Systematic investigation of the synaptic characteristics such as the excitatory postsynaptic current, paired-pulse facilitation index of the biaxially stretchable synaptic transistor under various levels of biaxial mechanical strain sets the operational foundation for stretchy distributed synapse arrays and neuromorphic cognitive skin devices. The biaxially stretchy arrays here achieved neuromorphic cognitive functions, including image memorization, long-term memorization, fault tolerance, programming, and erasing functions under 30% biaxial mechanical strain. The stretchy neuromorphic imaging sensory skin devices showed stable neuromorphic pattern reinforcement performance under both biaxial and nonuniform local deformation.

stretchy | distributed | synaptic transistor | neuromorphic | sensory skin

Cephalopod (e.g., squid, octopus, etc.) skin is not only a soft, deformable organ able to endure complex mode elastic deformations (bending, distension, stretch, twist, etc.; i.e., biaxially stretchy) but is also an unusual cognitive organ capable of visualizing, stealth, and camouflaging through complex biological processes of sensing, recognition, neurologic processing, and actuation in a distributed manner (1–7). Enabling distributed neurologic and cognitive functions in various soft emerging devices and systems, such as robotics, wearables, skin prosthetics, bioelectronics, etc. (8–18) would be a massive leap in their development. However, such development has not been reported. On the one hand, although several artificial camouflage skin devices have been recently developed (19–27), one missing yet critical feature of these devices is noncentralized neuromorphic processing and cognition capabilities. On the other hand, some of the recently developed soft synaptic devices, although shedding light on such biomimetic capabilities, cannot meet the critical requirements of biaxial elastic deformability and neurologic functions simultaneously like cephalopod skin. For example, soft synaptic transistors have been demonstrated to achieve brain-inspired computing (28, 29) and artificial nervous systems that are sensitive to touch (30, 31), sound (32), and light stimulation (33). Despite these advances, nevertheless, none of these devices can be biaxially stretched as reported elsewhere (34–37) while retaining their synaptic and neuromorphic functions.

Here, we report artificial neuromorphic cognitive skin devices based on arrayed, biaxially stretchable synaptic transistors constructed entirely out of elastomeric materials. The elastomeric synaptic transistor was constructed using an elastomeric poly(3-hexylthiophene-2,5-diyl nanofibrils/styrene-ethylene-butylene-styrene (P3HT-NFs/SEBS) semiconductor nanocomposite, an elastomeric conductor with silver nanowires modified with gold nanoparticles embedded in polydimethylsiloxane (PDMS) (denoted AuNPs-AgNWs/PDMS), and an elastomeric gate dielectric ion-gel. The devices constructed in this study exhibited neurologic synaptic behaviors such as excitatory postsynaptic currents (EPSC), paired-pulse facilitation (PPF), and memory characteristics similar to biological synapses. These synaptic characteristics were maintained even under 30% biaxial mechanical strain. A 5 × 5 array of the elastomeric synaptic transistors was demonstrated to achieve image memorization, long-term memorization, fault tolerance, and programming and erasing functions. A stretchy neuromorphic imaging sensory skin

Significance

Enabling distributed neurologic and cognitive functions in soft deformable devices, such as robotics, wearables, skin prosthetics, bioelectronics, etc., represents a massive leap in their development. The results presented here reveal the device characteristics of the building block, i.e., a stretchable elastomeric synaptic transistor, its characteristics under various levels of biaxial strain, and performances of various stretchy distributed neuromorphic devices. The stretchable neuromorphic array of synaptic transistors and the neuromorphic imaging sensory skin enable platforms to create a wide range of soft devices and systems with implemented neuromorphic and cognitive functions, including artificial cognitive skins, wearable neuromorphic computing, artificial organs, neurorobotics, and skin prosthetics.

Author contributions: H.S. and C.Y. designed research; H.S., S. J., A.T., S. J., H.J., B.K., S.P., H.-J.K., and C.Y. performed research; H.S., H.-J.K., and C.Y. analyzed data; and H.S., S.P., G.W., W.L., H.-J.K., and C.Y. wrote the paper.

The authors declare no competing interest.

This article is a PNAS Direct Submission.

[1] To whom correspondence may be addressed. Email: cmy5358@psu.edu or hjk@gnu.ac.kr.

This article contains supporting information online at http://www.pnas.org/lookup/suppl/doi:10.1073/pnas.2204852119/-/DCSupplemental.

Published June 1, 2022.

device based on a 5 × 4 sensing nodes array was developed that exhibited neuromorphic pattern reinforcement when stretched biaxially. The results reveal the key aspects of the characteristics of the stretchable elastomeric synaptic transistor as the building block and the performances of stretchy distributed neuromorphic skin devices.

Results

Fig. 1*A* illustrates the cephalopod skin–inspired soft neuromorphic cognitive system, which collects incident visual information and transmits synaptic signals for neuromorphic image data processing. Note that the neuromorphic cognitive skin devices developed in this work exhibit the unique characteristics of image sensing, preprocessing, and postprocessing. The building block of the arrayed skin device is a stretchable elastic synaptic transistor that can sustain under biaxial elastic deformations. It is noted that all the synaptic transistor and the skin devices were formed entirely out of elastomeric electronic materials. The elastomer materials were chosen mainly because they could offer biaxial stretchability and synaptic and neuromorphic functions simultaneously, similar to their biological counterparts, while other materials such as inorganics and polymers, which are intrinsically nonstretchable, require certain engineered architectures (38, 39) to enable stretchability. To construct the elastomeric synaptic transistor, an elastomeric semiconductor nanocomposite was prepared by forming a mechanically percolated P3HT-NFs mesh structure within the SEBS elastomer. The nanocomposite was synthesized using a previously described procedure (40). The surface morphology of the elastomeric P3HT-NFs/SEBS nanocomposite film under various levels of biaxial mechanical strain was confirmed based on photographs and optical microscope images, as shown in Fig. 1 *B* and *C*, respectively. Upon 30% biaxial mechanical strain, no visible cracks were observed on the elastomeric semiconducting nanocomposite thin film. Atomic force microscope (AFM) phase mode images of the elastomeric semiconductor nanocomposite thin film under 0% and 30% biaxial mechanical strain show the mesh structures of the P3HT-NFs within the SEBS elastomer (Fig. 1*D*). The P3HT-NFs retained their mesh structures with no noticeable cracks or damage under the 30% biaxial mechanical strain, facilitating electrical conductance. The elastomeric synaptic transistor was constructed by spin–coating the semiconducting nanocomposite over the elastomeric electrodes and

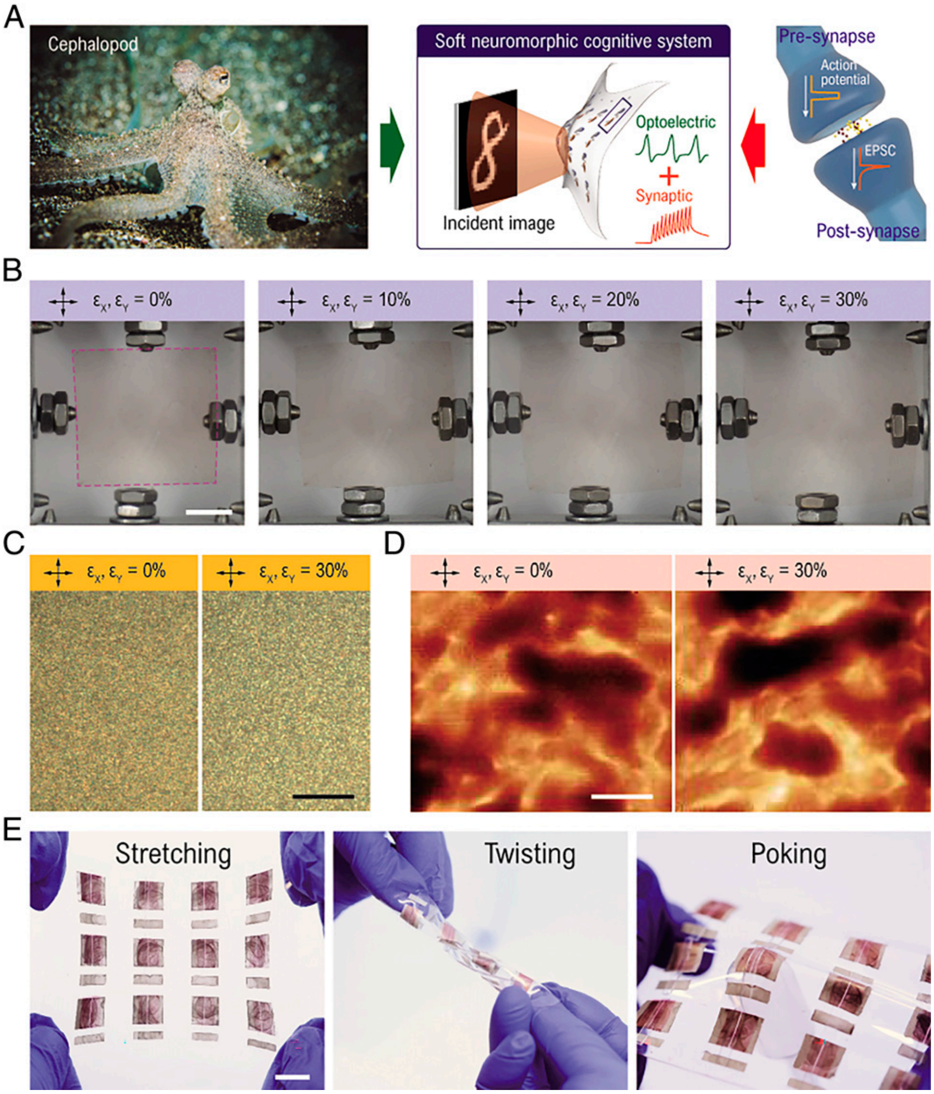

Fig. 1. Soft neuromorphic cognitive system. (*A*) Schematic illustrations of the soft neuromorphic cognitive system by combining the functions of cephalopod skin and biological synapse. Photographs (*B*), optical microscope images (*C*), and AFM phase mode images (*D*) of the P3HT-NFs/SEBS semiconductor nanocomposite under different levels of biaxial mechanical strain (Scale bars, 10 mm, 300 μm, and 200 nm, respectively). (*E*) Photographs of the 4 × 3 elastomeric synaptic transistor array under different types of mechanical deformations (Scale bar, 1 cm).

laminating the ion–gel dielectric over the semiconductor layer. A photograph of the elastomeric ion–gel is shown in *SI Appendix*, Fig. S1. The elastomeric electrode was prepared by embedding AgNWs in PDMS and performing galvanic replacement to conformally coat AuNPs on the surface of AgNWs, enabling an ohmic contact between the P3HT-NFs/SEBS semiconductor and the electrode (41, 42). The channel length and width of the fabricated device were 60 μm and 3 mm, respectively. The thicknesses of the P3HT-NFs/SEBS, ion–gel, and AuNPs-AgNWs were 350 nm, 140 μm, and 25 μm, respectively. The detailed manufacturing processes are described in *Materials and Methods*. Fig. 1*E* shows photographs of the elastomeric synaptic transistor array under different types of mechanical deformations, including biaxial mechanical stretching, twisting, and poking. The elastomeric synaptic device can deform without any physical damage or cracks, owing to the elastomeric nature of all materials used to fabricate the device.

Biaxially Stretchy Elastomeric Synaptic Transistors. Fig. 2*A* shows the schematic illustration of the elastomeric synaptic transistor, which is analogous to a biological synapse. During the device operation, the gate electrode serves as a presynapse, and the P3HT-NFs/SEBS semiconducting film between the source and drain electrodes performs as a postsynapse. A postsynaptic current is generated when a presynaptic pulse is applied to the gate electrode. The current through the P3HT-NFs/SEBS semiconducting channel is regarded as the synaptic weight and can be modulated via the flow of ions generated from the ion–gel by adjusting the presynaptic pulse conditions (43). We first evaluated the device's transfer characteristics and field–effect mobilities (μ_{FE}) under biaxial mechanical strain ranging from 0 to 30% (*SI Appendix*, Fig. S2). Upon 30% biaxial mechanical strain, which is equivalent to an areal strain of 69%, the μ_{FE} of the device decreased from 1 cm^2/V·s to 0.1 cm^2/V·s. Despite the performance degradation upon large biaxial mechanical stretching, the device retained its normal transfer characteristics, which is critical for achieving synaptic characteristics. Fig. 2*B* shows a set of optical photographs of the biaxially stretchy elastomeric synaptic transistors under 0 to 30% biaxial mechanical strain. The equivalent areal strain applied to the devices under 10%, 20%, and 30% biaxial mechanical strain are 21%, 44%, and 69%, respectively.

Fig. 2*C* shows the EPSCs of the developed synaptic transistors under 0 to 30% biaxial mechanical strain. A presynaptic pulse was applied with an amplitude of −3 V and a pulse width of 100 ms to characterize a single pulse-induced EPSC. The biaxial mechanical strain led to a decrease in EPSC from 140 μA (0% strain) to 132 μA, 119 μA, and 105 μA under 10%, 20%, and 30% biaxial mechanical strain, respectively. This outcome was attributed to the decrease in the ON current (I_{ON}) with the increasing mechanical strain, as presented in *SI Appendix*, Fig. S2. The I_{ON} was obtained, while applying the V_{GS} of −4 V with a constant V_{DS} of −1 V. A systematic analysis of the EPSC behaviors under 4 × 4 combinations (ε_X = 0%, 10%, 20%, 30% and ε_Y = 0%, 10%, 20%, 30%) of biaxial mechanical strain is presented in *SI Appendix*, Fig. S3.

Fig. 2*D* shows the set of EPSCs originating from the two presynaptic pulses under 0 to 30% biaxial mechanical strain. As shown in *SI Appendix*, Fig. S4, two successive presynaptic pulses with amplitudes of −3 V and a pulse interval of 100 ms were applied to evaluate the PPF index of the synaptic transistors (defined as PPF [%] = A_2/A_1 × 100%—i.e., the ratio between the peak intensities of the second EPSC [A_2] and the first EPSC [A_1]). The PPF index of the synaptic transistor ranged from 1.46 (0% strain) to 1.32, 1.23, and 1.16 under 10, 20, and 30% biaxial mechanical strain, respectively. The PPF index of the synaptic transistors under unidirectional and asymmetric mechanical strain can be found in *SI Appendix*, Figs. S5 and S6, respectively. The slight decrease in the PPF index originates from the disentangling of the polymer chain during stretching, which increases ion mobility (44). Fig. 2*E* presents the mapping data of a single pulse-induced EPSC peak, PPF index, and μ_{FE} with respect to the different levels of biaxial mechanical strain. The experimental results reveal that the decrease in the device's current resulted in a decrease in the EPSC peak values, PPF index, and μ_{FE} with increasing areal strain (45). Thus, the trend of these values in the map is in accordance with the areal strain. These results indicate that the synaptic transistor could retain synaptic function under large biaxial mechanical strain.

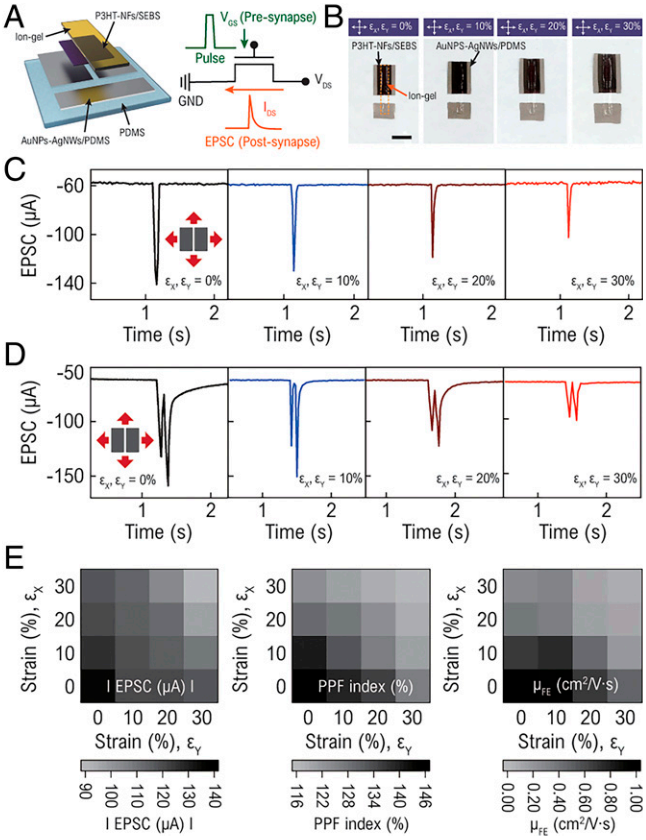

Fig. 2. Biaxially stretchy elastomeric synaptic transistors. (*A*) Schematic exploded view (*Left*) and the synaptic transistor's operational circuit (*Right*) (drain voltage (V_{DS}), gate voltage (V_{GS}), and ground (GND)). (*B*) Photographs of biaxially stretchy elastomeric synaptic transistors under different levels of biaxial mechanical strain (Scale bars, 2 mm). (*C*) Single pulse-induced EPSCs. (*D*) Two successive pulse-induced EPSCs. (*E*) Mapped EPSC peak, PPF index, and μ_{FE} under 0%, 10%, 20%, and 30% biaxial mechanical strain.

Memorization and Cognitive Functions in a Stretchy Synaptic Transistor Array. To examine the image memorization capability of the biaxially stretchy elastomeric synaptic transistor, we developed a 5 × 5 elastomeric synaptic transistor array (Fig. 3*A*). The array was constructed with the drains organized in a row and gates organized in a column. The detailed fabrication is described in *Materials and Methods*. Fig. 3*B* shows optical photographs of the elastomeric synaptic transistor array as fabricated (*Top*) and under 30% biaxial mechanical strain (*Bottom*) ($\varepsilon_{X'}$, $\varepsilon_{Y'}$ = ~42%), confirming that there are no noticeable failures in the array. To characterize the image memorization

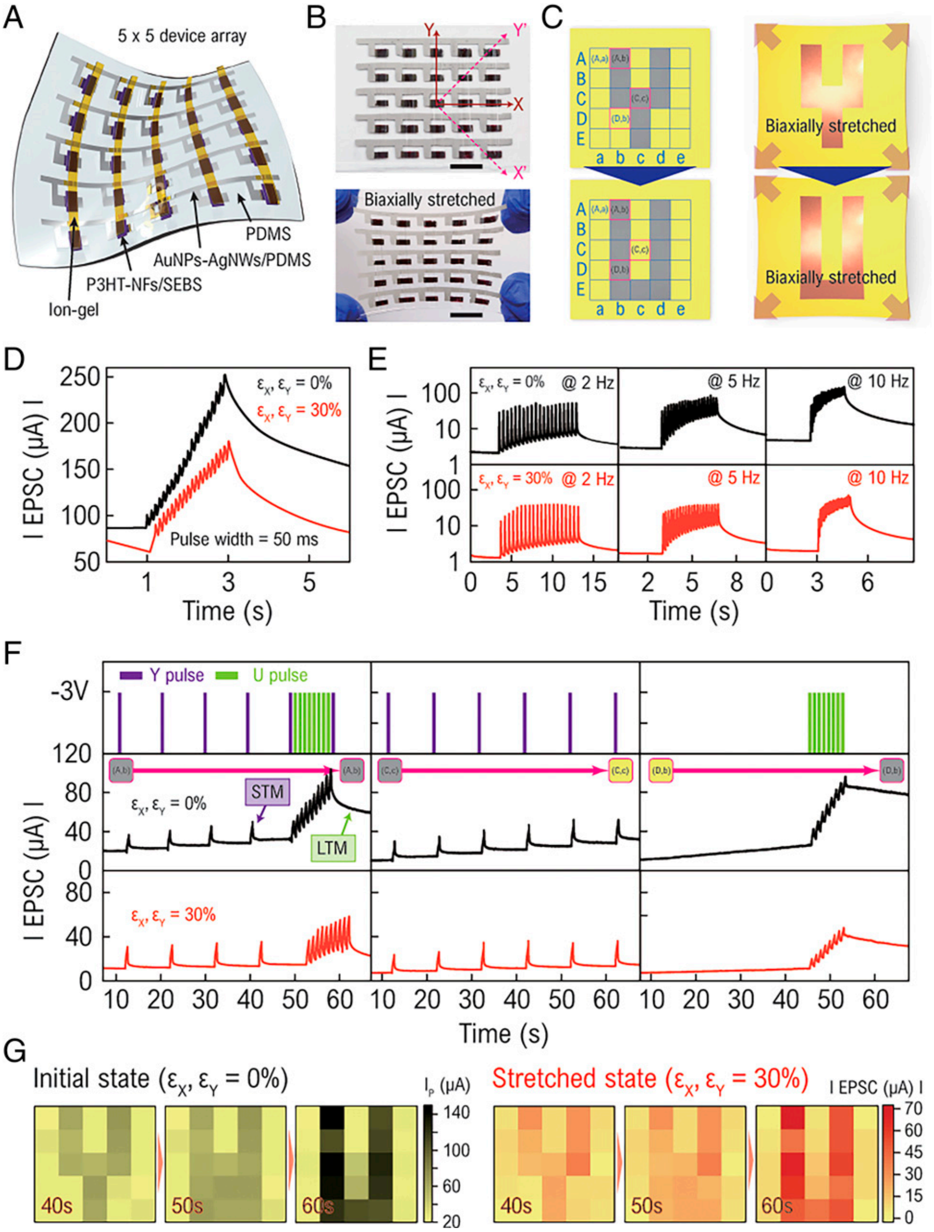

Fig. 3. Biaxially stretchy elastomeric synaptic transistor array. (*A*) The schematic of a 5 × 5 array of elastomeric synaptic transistors. (*B*) Optical images of a 5 × 5 array of elastomeric synaptic transistors without and with 30% biaxial mechanical strain. (*C*) Schematic illustration of image memorization of the letters “Y” and “U.” (*D* and *E*) Memory characteristics without (black) and with (red) 30% biaxial mechanical strain in representative EPSC results (*D*) and with variable frequencies (2, 5, and 10 Hz) (*E*). (*F*) Three EPSC results in image memorization without (black) and with (red) 30% biaxial mechanical strain. (*G*) Mapped images of a 5 × 5 array of elastomeric synaptic transistors without (black) and with (red) 30% biaxial mechanical strain.

performance of the array, various presynaptic pulses were applied on each pixel device to acquire and memorize letters of the alphabet (e.g., “Y” and “U”). The gray-colored pixels in Fig. 3*C* (*Left*) represent the location of the application of the presynaptic pulse, and the yellow-colored pixels show where no pulses were applied. Each pixel in the array is denoted as (A,a) to (E,e). The red-colored pixels in Fig. 3*C* (*Right*) show the biaxially stretched state of the array.

The synaptic memory characteristics of the elastomeric synaptic transistors were examined. The measurement was conducted by acquiring the EPSC while applying 20 successive presynaptic pulses with 50 ms pulse widths and −3 V amplitudes. Fig. 3*D* shows the EPSC under 0% (black) and 30% (red) biaxial mechanical strain, which simultaneously demonstrates the short-term memory (STM) and long-term memory (LTM) characteristics. Under 30% biaxial mechanical strain, we observed a decrease in the overall EPSC as well as a long-term weight change (i.e., $\Delta W/W_0$) from 1.88 (ε_X, ε_Y = 0%) to 1.21 (ε_X, ε_Y = 30%). W_0 and ΔW represent the initial EPSC and the EPSC change after the presynaptic pulse, respectively. The synaptic transistors were then subjected to presynaptic pulses with various frequencies (2, 5, and 10 Hz) to observe the frequency dependence of the STM and LTM characteristics. Fig. 3*E* shows the memory characteristics under 0% (*Top*, black) and 30% (*Bottom*, red) biaxial mechanical strain. As the pulse frequency increased from 2 to 10 Hz, $\Delta W/W_0$ increased from 0.78 to 1.88 under 0% strain and from 0.61 to 1.21 under 30% biaxial mechanical strain. Furthermore, the synaptic transistors exhibited memory performances regardless of the presynaptic pulse frequency (1, 3, or 15 Hz) and the biaxial mechanical strain (up to 30%) (*SI Appendix*, Fig. S7). The experimental results suggest that the elastomeric synaptic transistors not only exhibit superior STM and LTM characteristics but also retain the performance at up to 30% biaxial mechanical strain.

To achieve STM, an image of the letter "Y" was memorized by applying the voltage with a 500 ms pulse width, −3 V amplitude, and 0.1 Hz pulse frequency six times, as marked with the Y pulse (purple bar) in Fig. 3*F*. The voltage was applied to nine locations to form a Y-shaped image marked with gray-colored pixels, e.g., (A,b) and (C,c). The array's STM to LTM transition performance was achieved by memorizing the letter "U" immediately after the "Y" STM. The LTM characteristics were achieved by applying the same pulse width (500 ms) and amplitude (−3 V) but at a faster frequency (1 Hz) eight times between the fifth and sixth pulses of the Y pulse (see the U pulse, green bar in Fig. 3*F*). Detailed information on the input signals for memorizing the letters "Y" and "U" is presented in *SI Appendix*, Fig. S8.

The graphs in the first column of Fig. 3*F* show the STM and LTM characteristics of pixels (A,b) (indicated with a pink rectangle) undergoing the sequential application of the Y (purple bar) and U (green bar) pulses under 0% (black) and 30% (red) biaxial mechanical strain. Upon the application of the presynaptic Y pulse, the EPSC showed an STM characteristic up to the fifth pulse regardless of the mechanical strain. With the application of U pulses soon after the fifth Y pulse, the EPSC was substantially increased up to the last input for the letter "U" and persisted for 20 s from the last input, reflecting a successful transition performance from STM to LTM. The color of the pixel (A,b) remained gray because this pixel was maintained in a memorized state during the image transition from "Y" to "U." The outcome was consistent under 30% biaxial mechanical strain.

The second column of Fig. 3*F* shows the EPSC results obtained during Y pulse application at the initial state (0% strain) and under 30% biaxial mechanical strain. Pixel (C,c) was erased during the transition from "Y" to "U," so no U pulse was applied. The synaptic transistor demonstrated an STM performance when applying six sequential Y pulses, resulting in satisfactory pixel-erasing characteristics of (C,c). The third column shows the EPSC results of pixel (D,b), where the memorization was developed with an application of U pulses during the transition. The EPSC results confirm that the LTM characteristics were well-realized under 0% and 30% biaxial mechanical strain.

Fig. 3*G* (*Left*) shows the complete information captured during the image transition from "Y" to "U" at 40, 50, and 60 s. The image of the letter "Y" appears after applying the first five pulses. At 50 s, the process of converting from "Y" to "U" is revealed. After applying U pulses at a relatively high frequency, the image of the letter "Y" decays and the image of the letter "U" is enhanced, resulting in a more distinct "U" image after 60 s (contrast enhancement). The same tendency was observed in the biaxially stretched array of elastomeric synaptic transistors (Fig. 3*G*, *Right*). The results show that our elastomeric synaptic transistor array achieved image memorization and STM/LTM transition characteristics, regardless of the biaxial mechanical strain (up to 30%).

Additional features of the elastomeric synaptic transistor array, including long-term memorization, fault tolerance, and programming/erasing, are summarized in Fig. 4. The array was subjected to 10 sets of 10 successive presynaptic pulses with pulse widths of 167 ms, pulse frequencies of 3 Hz, amplitudes of −3 V, and train intervals of 5 s to examine the long-term memorization capability via the EPSC results (Fig. 4*A*). The EPSC values increased with increasing pulse trains (Fig. 4*B*). After 10 trains, the EPSC increased from 9.82 to 1,190 μA under 0% strain and from 7.59 to 468 μA under 30% biaxial mechanical strain. Furthermore, $\Delta W/W_0$ increased with increasing pulse trains for arrays with and without 30% biaxial mechanical strain (Fig. 4*C*). Specifically, $\Delta W/W_0$ increased from 11.7 to 155.8 with 0% strain and from 8.5 to 46.7 with 30% biaxial mechanical strain.

The EPSC maps obtained from a 5 × 5 elastomeric synaptic transistor array with increasing pulse trains (up to 10) are shown in Fig. 4*D*. The array shows an increase in the EPSC with increasing pulse trains. Notably, 15 min after the 10th train, the EPSC value was greater than the initial EPSC due to ion accumulation at the interface between the P3HT-NFs/SEBS and ion–gel (46). A similar trend was observed under 30% biaxial mechanical strain (*SI Appendix*, Fig. S9). The unique capabilities of the constructed synaptic transistor array enabled reliable memory operations with stable mechanical sustainability.

To examine the fault tolerance of the array against incorrect input signals, which can be collected due to noise or error, the resilience of the EPSC output was validated by applying a voltage to two pixels at the wrong location, as shown in Fig. 4*E*. The test consisted of four steps, the first of which was to apply a voltage to M-shaped pixels (first train: true input), followed by three successive trains each of which moved two pixels from the M shape (second, third, and fourth trains: false input). Regardless of the input at the wrong pixels, the EPSC of the M shape became stronger during the progression from the second to the fourth train. Even though the array was subjected to multiple false input pulses during the test, the objective picture of the letter "M" was easily visualized following the fourth train. Thus, the array is responsive to true pulses and insensitive to false pulses as the train progresses.

Next, we assessed the potentiation and depression behaviors to verify the programming and erasing capability of the synaptic transistor array. Increases and decreases in the EPSC level, controlled by applying different amplitudes of presynaptic pulses, are used to program and erase the array, respectively. Fig. 4*F* shows an increased EPSC level (i.e., program) by applying 60 successive presynaptic pulses with pulse widths of 500 ms, pulse frequencies of 2 Hz, and amplitudes of −4 V. To reduce (i.e., erase) the level of EPSC to the initial state, we applied 60 successive presynaptic pulses with the same pulse widths and frequencies but 6 V amplitudes. The red line in Fig. 4*F* represents the EPSC results obtained under 30% biaxial mechanical strain, which exhibited stable programming and erasing performances. Fig. 4*G* shows the EPSC decay with respect to the number of pulses under no strain and 30% biaxial mechanical strain. The findings demonstrate that applying 60 presynaptic pulses is sufficient to reset the EPSC level to the initial state, deleting the previously memorized data. The pixelated letters "L," "T," and "M" were consecutively programmed and erased in the above-stated way, as illustrated in Fig. 4*H*. *SI Appendix*, Fig. S10 depicts the outcome under 30% biaxial mechanical strain. Overall, the results reveal that the synaptic transistor array has considerable potential in applications such as stretchy neuromorphic cognitive systems.

Biaxially Stretchy Neuromorphic Imaging Sensory Skin Device. Fig. 5*A* shows the block diagrams of the conceptual image process flow when a soft, neuromorphic cognitive system perceives the visual information of familiar and strange objects. In a dangerous situation, the frequently seen (i.e., familiar [shark]) objects evoke the learning and training process of the object images, leading to a deeper impression, which results in

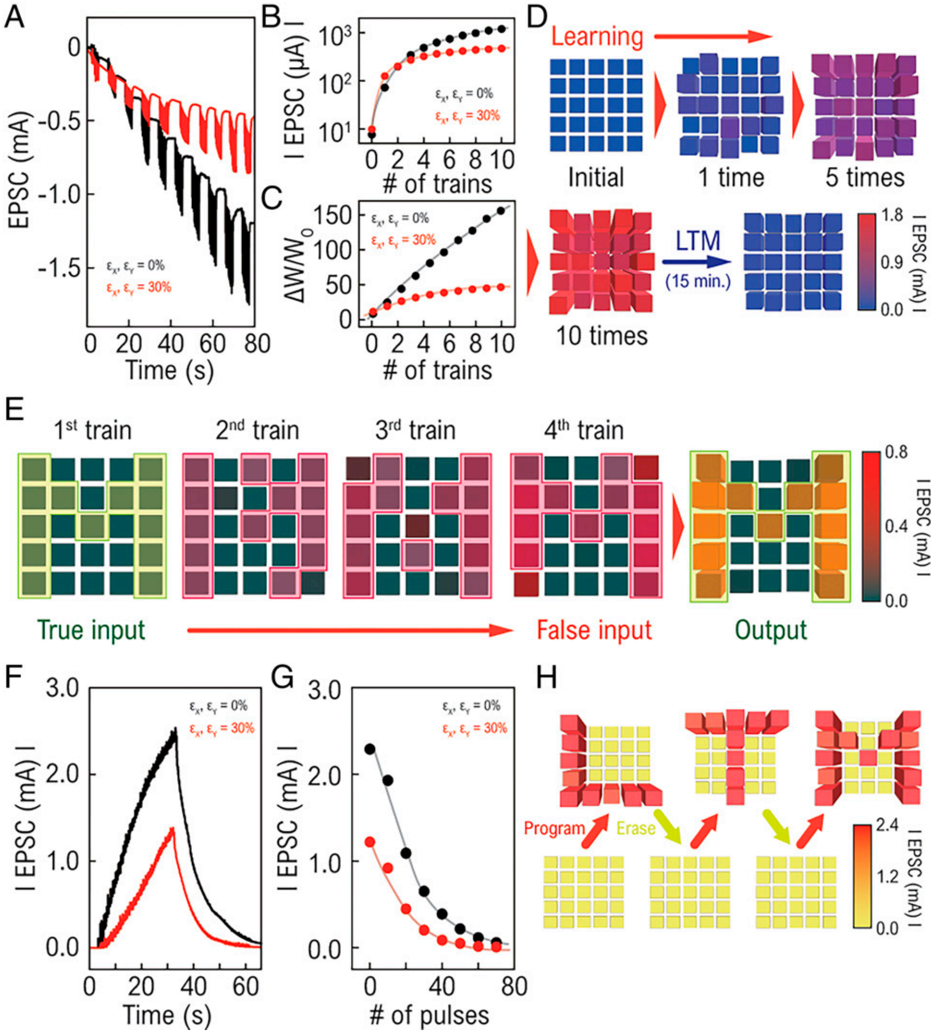

Fig. 4. Neuromorphic cognitive features of the biaxially stretchy array. (*A*) EPSC values over 10 successive presynaptic pulses (pulse width: 167 ms; pulse frequency: 3 Hz; amplitude: −3 V; train interval: 5 s). The EPSC (*B*) and long-term weight change (*C*) with increasing numbers of trains without (black) and with (red) 30% biaxial mechanical strain. (*D*) Mapped EPSC results of a 5 × 5 array of elastomeric synaptic transistors with increasing numbers of trains. (*E*) The fault-tolerance capability of a 5 × 5 array of elastomeric synaptic transistors. (*F*) EPSC from 60 programming pulses and erasing pulses without (black) and with (red) 30% biaxial mechanical strain. (*G*) EPSC decay with increasing numbers of erase pulses without (black) and with (red) 30% biaxial mechanical strain. (*H*) Programmed and erased images of the letters "L," "T," and "M.".

clear image perception. In contrast, occasionally seen (i.e., strange [Nemo]) objects are processed without LTM, leading to faint synaptic image signals and blurred image perception. To demonstrate the function of the soft neuromorphic imaging sensory system, we developed the neuromorphic imaging sensory skin device in a fully elastomeric manner, employing soft electronic devices, including a resistor, the synaptic transistor, and photodetector. Fig. 5*B* shows a schematic exploded view of the stretchy neuromorphic imaging sensory skin device, which consists of three layers: the patterned electrode array (*Bottom*), the stretchy resistor array (*Middle*), and the stretchy photodetector and synaptic transistor array (*Top*). Note that the final device is encapsulated with a PDMS layer. The via holes are formed for the vertical interconnects between the layers. *SI Appendix*, Fig. S11 shows the circuit diagram of the 5 × 4 arrayed neuromorphic imaging sensory skin device. In the neuromorphic circuit, postsynaptic current is measured while both V_{D1} and $V_{D2\ (n)}$ are applied as the supply voltage of the photovoltaic divider and the drain voltage of the synaptic transistor, respectively.

The stretchy voltage divider comprises an organic photodetector and a load resistor, which converts the light information into a voltage output (47). The right illustrated image in Fig. 5*B* shows the developed organic photodetector device structure. The bilayer of AuNPs-AgNWs/PDMS and Poly(3,4-ethylenedioxythiophene)-poly(styrenesulfonate) (PEDOT:PSS) acts as a transparent conducting electrode designed to acquire the incident light (48). The vertical structure was selected to provide a large I_{ON} and be compatible with the synaptic transistor (49). *SI Appendix*, Fig. S12 shows the schematic of the photodetector energy–level diagram. A planar geometry-based resistor made of organic semiconductor has too high of a resistance to make it matchable with the photodetector and synaptic transistor. Since the multiwalled carbon nanotube (m-CNT) has a much lower resistance (50), doping m-CNT realized by dry transfer could substantially reduce the resistance of the resistor (51). Note that the increase in conductivity is because m-CNTs shorten the transport distance in the channel area, which leads to higher effective conductivity. Thus, the load resistor was fabricated using m-CNT–doped P3HT-NFs/SEBS. The m-CNT–doped P3HT-NFs/SEBS layer showed a significantly increased current than that of P3HT-NFs/SEBS alone, which has a similar current level as the I_{OFF} of the photodetector. The *I*–*V* curve of the load resistor without and with m-CNT doping (0.1 wt%) is shown in *SI Appendix*, Fig. S13.

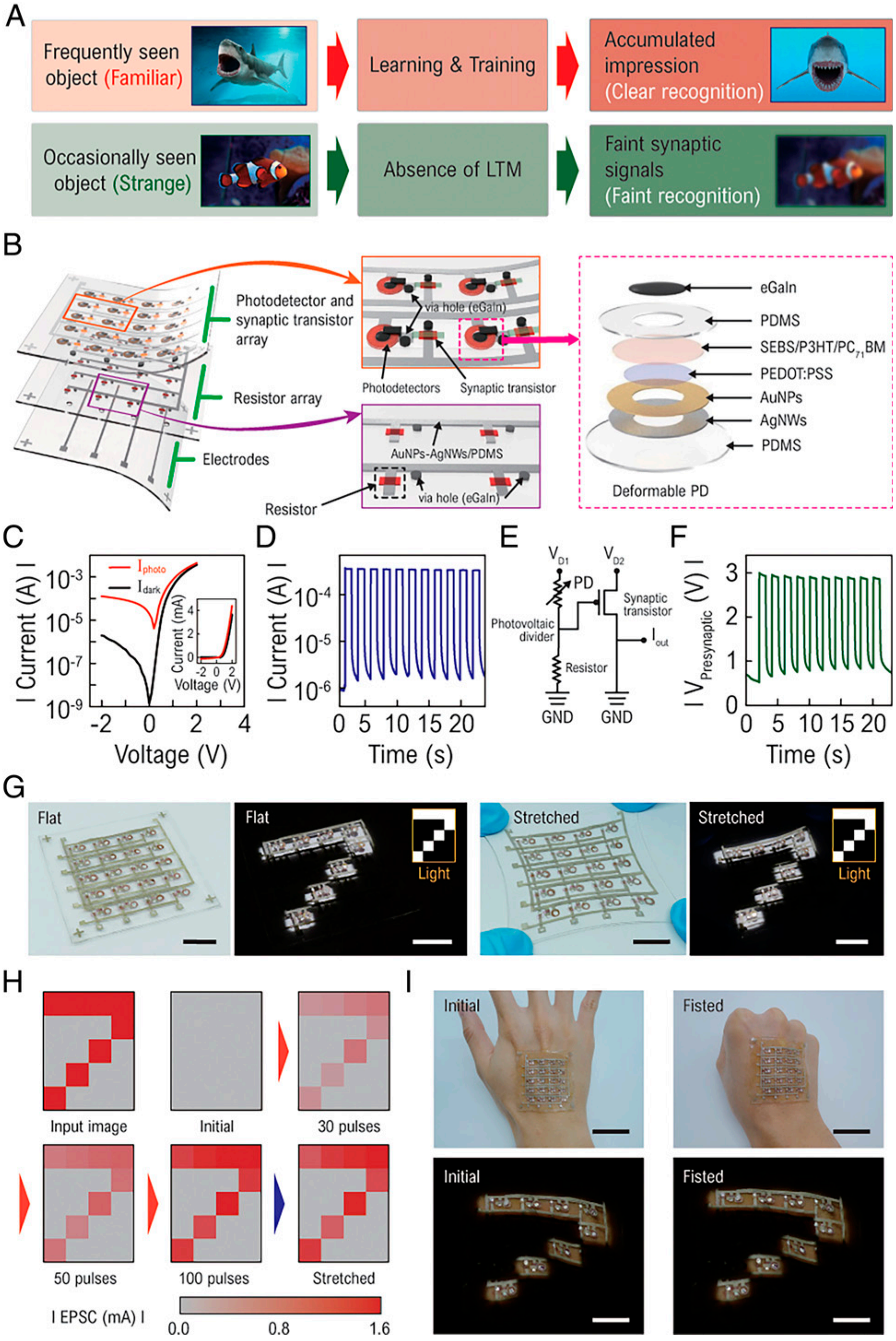

Fig. 5. Biaxially stretchy neuromorphic imaging sensory skin device. (*A*) Block diagrams of the soft neuromorphic cognitive system operating flow when familiar (red, Shark) and strange (green, Nemo) objects are observed. (*B*) Schematic exploded view of the stretchy neuromorphic imaging sensory skin device. Inset schematics (*Right*) show detailed device structure of the array and the organic photodetector. (*C* and *D*) *I–V* curve and dynamic photocurrent responses of the organic photodetector. (*E* and *F*) Circuit diagram of an individual sensing pixel and corresponding dynamic voltage response under pulsed light illumination. (*G*) Optical photographs of the neuromorphic imaging sensory skin device at initial (*Left*) and biaxially stretched (*Right*) states before and after "7"-shaped light illumination (Scale bars, 2 cm). (*H*) Mapped photoresponsive EPSC of the stretchy neuromorphic imaging sensory skin device with respect to the number of light pulses. (*I*) Optical photographs of the stretchy neuromorphic imaging sensory skin device adhered on human skin at initial and fisted (stretched) state before (*Top*) and after (*Bottom*) the light illumination (Scale bars, 3 cm [*Top*] and 10 mm [*Bottom*]).

As presented in Fig. 5*C*, the fabricated photodetectors show a typical photodiode *I–V* behavior, with an I_{ON}/I_{OFF} ratio of 2.4×10^2. The photodetector exhibited a stable dynamic performance under the pulsed light with a width of 1s, a frequency of 0.5 Hz, and an intensity of 138.7 klx (Fig. 5*D*). Fig. 5*E* shows the circuit diagram of an individual sensing pixel consisting of the photovoltaic divider and the synaptic transistor. The photovoltaic divider performance is shown in Fig. 5*F*. The measurement was conducted by applying a pulsed light with the same characteristics. Upon pulsed illumination, the voltage oscillated from −1 to −3 V, which is adequate for operating the synaptic transistor.

To demonstrate the neuromorphic imaging cognition capabilities, different numbers of pulses of "7"-shaped light, i.e., 0, 30, 50, 100, and 100 (stretched case) pulses, were applied to the array. The duty cycle of the successive pulses was 50% with a pulse frequency of 0.5 Hz. The EPSC was obtained under the pulsed light with a duration of 1 s and a period of 5 s at a V_{D1} of −3 V and a V_{D2} of −1 V. Fig. 5*G* shows a stretchy neuromorphic imaging sensory skin device conformally adhered to the flat surface (*Left*) and biaxially stretched (*Right*) before and after the "7"-shaped light illumination. Fig. 5*H* shows an EPSC map, exhibiting an increased EPSC with increasing numbers of light pulses. The "7"-shaped EPSC increased with an increasing number of light pulses up to 100, demonstrating a successful presentation of neuromorphic pattern reinforcement using the skin device developed in this work. Moreover, no significant degradation was observed under 30% biaxial mechanical strain. Thus, the function of neuromorphic pattern reinforcement was successfully achieved in the neuromorphic imaging sensory skin device, which reflects a deeper impression of the perceived image. Fig. 5*I* is the optical photographs of the skin device adhered to a human hand. The device did not show any material or structural failure, resulting in stable neuromorphic pattern reinforcement performances under repetitive opening and fisting hand motions.

Discussion

To enable stretchable distributed neuromorphic and cognitive functions in a soft skin device, the building block, i.e., a stretchable elastomeric synaptic transistor, was entirely developed using elastomeric electronic materials. Using elastomeric rubbery materials for all the device components is the key to realizing a biaxially stretchy elastomeric synaptic transistor and its array-based neuromorphic devices. The elastomeric synaptic transistor was biaxially stretched up to 30% and exhibited a full set of synaptic behaviors, including EPSC, PPF, and memory characteristics similar to the biological synapse. Stretchy distributed neuromorphic devices based on biaxially stretchable synaptic transistor arrays, memorization, and cognitive functions were successfully exhibited, including image memorization, long-term memorization, fault tolerance, and programming/erasing function under 30% biaxial mechanical strain. To implement the neuromorphic processing and cognition capability in a stretchy distributed device, a fully stretchy neuromorphic imaging sensory skin device based on a 5 × 4 sensing node array was constructed. Its neuromorphic pattern reinforcement function was validated even when the skin device was deformed nonuniformly.

With the recent surge of smart skin devices (52, 53), implementing neuromorphic functions into these devices open the door for a future direction toward more powerful biomimetics limited not just to neuromorphic imaging but also to multimodal somatic sensing and many others. By leveraging neuromorphic hardware and computing power with sensing technologies, e.g., a soft elastic system in this work, a broad range of benefits, such as high-accuracy, low-cost sensing and recognition could be easily reached. The methodology of implementing neuromorphic functions into smart skin devices as shown in this work could be exploited into many other areas, such as wearable neuromorphic computing (28), artificial organs (54), neurorobotics (55), and skin prosthetics (53) toward the next-generation intelligent systems.

Materials and Methods

Preparation of the Elastomeric Conductor. First, a polyimide (PI) stencil mask was prepared on a precleaned glass using a programmable cutting machine (Silhouette Cameo). The 20 mg/mL AgNWs solution in EtOH (ACS Materials, AgNW-120) was drop-casted on the PI/glass substrate and dried for 5 min at 70 °C. The drop-casting and drying process was repeated until the conductor exhibited sufficiently low electrical resistance. The AgNWs conductor was then annealed at 200 °C for 30 min for the AgNWs welding process. The PDMS solution (10:1 [wt/wt] prepolymer/curing agent) was then spin-coated at 250 rpm for 60 s on the patterned AgNWs conductor. After the samples were cured in the oven at 95 °C for 4 h, the PDMS was carefully peeled off the glass to prepare the stretchable AgNWs/PDMS conductor. To form an ohmic contact between the AgNWs electrodes and the P3HT semiconductor, AuNPs were conformally coated on the AgNWs via galvanic exchange. $HAuCl_4 \cdot 3H_2O$ aqueous solution (5 mg/mL) was dropped on the AgNWs/PDMS electrode surface for 2 min for the Ag–Au galvanic exchange reaction. AgCl residue was removed by placing NH_4OH solution on the electrodes for 1 min, followed by deionized water rinsing to complete the AuNPs-AgNWs/PDMS conductor manufacturing process.

Preparation of the Elastomeric Semiconductor. Prior to the blending process, P3HT/toluene solution (2 mg/mL) was kept in a −20 °C chamber for 1 h to form self-assembled P3HT nanofibrils. The SEBS/toluene solution (20 mg/mL) was then blended 1:1 (wt/wt) with the P3HT-NFs/toluene solution. The P3HT-NFs/SEBS semiconductor was fabricated by spin-casting at 2,000 rpm for 60 s on the PDMS substrate, followed by thermal annealing at 90 °C for 10 min.

Preparation of the Elastomeric Dielectric. PVDF-HFP, EMIM-TFSI, and acetone were mixed at a weight ratio of 1:4:7 at 80 °C for 8 h. The ion–gel solution was casted on precleaned glass and cured in a vacuum oven at 70 °C for 12 h. The cured ion–gel could be easily cut into several pieces as desired and laminated on the devices to use as a dielectric layer.

Preparation of the m-CNT–Doped Elastomeric Semiconductor for the Load Resistor. m-CNTs were dispersed in 1,2-dichlorobenzene (2 mg/mL) by tip sonication for 1 h, followed by bath sonication for 5 h. The m-CNT suspension was spin-coated on precleaned glass at 3,000 rpm for 60 s and dried at 90 °C for 10 min. The m-CNTs on glass were placed in contact with the P3HT-NFs/SEBS semiconductor to transfer m-CNTs onto the semiconductor layer.

Preparation of the Elastomeric PEDOT:PSS Film. Aqueous PEDOT:PSS solution (CleviosTM PH1000, Heraeus) was mixed with a 3 wt% surfactant (Triton X-100, Sigma-Aldrich) and stirred for 12 h. The solution was spin-coated on the surface-modified PDMS substrate at 2,000 rpm for 60 s and dried at 90 °C for 10 min to form the PEDOT:PSS film.

Preparation of the Elastomeric Bulk Heterojunction Blend Film. A blending solution of SEBS:P3HT:$PC_{71}BM$ was prepared at a 2:1:1 weight ratio. A chlorobenzene solution of the elastomeric bulk heterojunction (BHJ) with a concentration of 40 mg/mL was stirred at 700 rpm for 24 h. Both p-type and n-type materials were obtained from Millipore Sigma. The elastomeric BHJ film was formed on the PEDOT:PSS film by spin-coating at 800 rpm for 30 s, followed by thermal annealing at 145 °C for 30 min.

Fabrication of the Biaxially Stretchy Elastomeric Synaptic Transistors and Arrays. First, the AuNPs-AgNWs/PDMS conductor (source and drain electrode) was prepared as described in "Preparation of the Elastomeric Conductor" above. The P3HT-NFs/SEBS film was formed on the channel region by spin-coating with a Kapton film-based shadow mask. Finally, a piece of the ion–gel dielectric (∼150 μm) was laminated on the P3HT-NFs/SEBS film to complete the fully elastomeric synaptic transistor. All elastomeric synaptic devices were fabricated following the same procedure with different electrode patterns.

Fabrication of the Stretchy Photodetector. The patterned AuNPs-AgNWs/PDMS conductor was prepared as described in "Preparation of the Elastomeric Conductor" above. The PEDOT:PSS film was formed on top of a patterned AuNPs-AgNWs/PDMS conductor that was treated with UV-O_3 for 20 min and immersed in APTES solution (3 wt% in deionized water) for 20 min by spin-coating the mixture solution through a Kapton film-based shadow mask. After removing the shadow mask, the resulting film was annealed on a hot plate at 140 °C for 10 min to enhance its electrical conductivity. The elastomeric BHJ film was formed on the PEDOT:PSS film in the same manner as described in "Preparation of the Elastomeric Bulk Heterojunction Blend Film" above. A patterned PDMS layer was formed on the elastomeric BHJ film to prevent electrical connection between the bottom and top electrodes of the photodetector. Liquid metal was patterned on the elastomeric BHJ film to complete the stretchy photodetector.

Fabrication of Biaxially Stretchy Neuromorphic Imaging Sensory Skin Device. The stretchy neuromorphic imaging sensory skin device fabrication started with the preparation of a stretchy AgNWs/PDMS electrode array as described in *Materials and Methods* and shown in *SI Appendix*, Fig. S14. To prepare a layer with a resistor array, the m-CNT–doped P3HT-NFs/SEBS-based elastomeric film was patterned on another AgNWs/PDMS electrode array, and via holes were formed using a hand–puncher for interconnection between layers. The detailed process is schematically shown in *SI Appendix*, Fig. S15. The layer with the resistor array was assembled with the prepared electrode array by heating at 90 °C for 1 h after exposing it under a UV-O_3 lamp (HBK Inc.), which provides for strong covalent bonding between each PDMS-based substrate (56). Then, the liquid metal was injected into the via holes to achieve interconnection between the two layers. The last layer was prepared by fabricating a stretchy photodetector and synaptic transistor array (*SI Appendix*, Fig. S16). The via holes were formed for vertical interconnects. The channel dimensions of the photodetector (r) and resistor (W/L) were 1 mm and 1,350 μm/100 μm, respectively. Finally, the photodetector and synaptic transistor array was assembled with the prepared layer containing the resistor and electrode array, followed by the injection of liquid metal into the via holes to finalize the fabrication of the stretchy neuromorphic imaging sensory skin device (*SI Appendix*, Fig. S17). Note that a homemade alignment system was used to align, stack, and assemble each layer. The overlaid architecture for each layer of the skin device and the cross-sectional image of individual light sensing area are presented in *SI Appendix*, Fig. S18.

Material Characterization and Device Measurements. The I–V curves and EPSCs of the devices were characterized using a probe station (H100, Signatone) equipped with a semiconductor analyzer (4200-SCS, Keithley). The presynaptic pulse from a function generator (DG4062, Rigol) was applied to the gate electrode. The EPSC was measured by applying a constant V_{ds} of -1 V between the source and the drain using a power supply (1627A, BK Precision).

Data Availability. All study data are included in the article and/or *SI Appendix*.

ACKNOWLEDGMENTS. C.Y. thanks the Office of Naval Research for financial support (Grant N00014-18-1-2338) under the Young Investigator Program and acknowledges the NSF grants of CAREER (1554499), EFRI (1935291), and CPS (1931893).

Author affiliations: [a]Department of Engineering Science and Mechanics, Pennsylvania State University, University Park, PA 16802; [b]Materials Science and Engineering Program, University of Houston, Houston, TX 77204; [c]Department of Mechanical Engineering, University of Houston, Houston, TX 77204; [d]School of Mechanical and Aerospace Engineering, Gyeongsang National University, Jinju 52828, Republic of Korea; [e]Tsinghua-Berkeley Shenzhen Institute, Institute of Materials Research, Tsinghua Shenzhen International Graduate School, Tsinghua University, Shenzhen 518000, China; [f]School of Physical Science and Technology, Lanzhou University, Lanzhou 730000, China; [g]Department of Biomedical Engineering, Pennsylvania State University, University Park, PA 16802; [h]Department of Materials Science and Engineering, Pennsylvania State University, University Park, PA 16802; and [i]Materials Research Institute, Pennsylvania State University, University Park, PA 16802

1. C. L. Huffard, F. Boneka, R. J. Full, Underwater bipedal locomotion by octopuses in disguise. *Science* **307**, 1927 (2005).
2. R. T. Hanlon, J. B. Messenger, *Cephalopod Behaviour* (Cambridge University Press, 2018).
3. L. M. Mäthger, E. J. Denton, N. J. Marshall, R. T. Hanlon, Mechanisms and behavioural functions of structural coloration in cephalopods. *J. R. Soc. Interface* **6**, S149–S163 (2009).
4. J. A. Mather, L. Dickel, Cephalopod complex cognition. *Curr. Opin. Behav. Sci.* **16**, 131–137 (2017).
5. R. Hanlon, Cephalopod dynamic camouflage. *Curr. Biol.* **17**, R400–R404 (2007).
6. J. B. Messenger, Cephalopod chromatophores: Neurobiology and natural history. *Biol. Rev. Camb. Philos. Soc.* **76**, 473–528 (2001).
7. L. M. Mäthger, S. B. Roberts, R. T. Hanlon, Evidence for distributed light sensing in the skin of cuttlefish, Sepia officinalis. *Biol. Lett.* **6**, 600–603 (2010).
8. C. Yu *et al.*, Adaptive optoelectronic camouflage systems with designs inspired by cephalopod skins. *Proc. Natl. Acad. Sci. U.S.A.* **111**, 12998–13003 (2014).
9. C. Xu, G. T. Stiubianu, A. A. Gorodetsky, Adaptive infrared-reflecting systems inspired by cephalopods. *Science* **359**, 1495–1500 (2018).
10. F. Hartmann, M. Drack, M. Kaltenbrunner, Meant to merge: Fabrication of stretchy electronics for robotics. *Sci. Robot.* **3**, eaat9091 (2018).
11. B. S. Kim *et al.*, Electrothermal soft manipulator enabling safe transport and handling of thin cell/tissue sheets and bioelectronic devices. *Sci. Adv.* **6**, eabc5630 (2020).
12. C. Larson *et al.*, Highly stretchable electroluminescent skin for optical signaling and tactile sensing. *Science* **351**, 1071–1074 (2016).
13. H. Shim, K. Sim, F. Ershad, S. Jang, C. Yu, Recent advances in materials and device technologies for soft active matrix electronics. *J. Mater. Chem. C Mater. Opt. Electron. Devices* **8**, 10719–10731 (2020).
14. H. Shim, S. Jang, C. Yu, High-resolution patterning of organic semiconductors toward industrialization of flexible organic electronics. *Matter* **5**, 23–25 (2022).
15. K. He *et al.*, An artificial somatic reflex arc. *Adv. Mater.* **32**, e1905399 (2020).
16. J. Kim *et al.*, Stretchable silicon nanoribbon electronics for skin prosthesis. *Nat. Commun.* **5**, 5747 (2014).
17. Y. Lee *et al.*, Stretchable organic optoelectronic sensorimotor synapse. *Sci. Adv.* **4**, eaat7387 (2018).
18. X. Zhang *et al.*, An artificial spiking afferent nerve based on Mott memristors for neurorobotics. *Nat. Commun.* **11**, 51 (2020).
19. S. Hong, S. Shin, R. Chen, An adaptive and wearable thermal camouflage device. *Adv. Funct. Mater.* **30**, 1909788 (2020).
20. T. Han, X. Bai, J. T. Thong, B. Li, C. W. Qiu, Full control and manipulation of heat signatures: Cloaking, camouflage and thermal metamaterials. *Adv. Mater.* **26**, 1731–1734 (2014).
21. H. Zhu *et al.*, Multispectral camouflage for infrared, visible, lasers and microwave with radiative cooling. *Nat. Commun.* **12**, 1805 (2021).
22. T. Wu *et al.*, A thermochromic hydrogel for camouflage and soft display. *Adv. Opt. Mater.* **8**, 2000031 (2020).
23. K. Chen *et al.*, Bioinspired dynamic camouflage from colloidal nanocrystals embedded electrochromics. *Nano Lett.* **21**, 4500–4507 (2021).
24. S. Chandra, D. Franklin, J. Cozart, A. Safaei, D. Chanda, Adaptive multispectral infrared camouflage. *ACS Photonics* **5**, 4513–4519 (2018).
25. M. Li, D. Liu, H. Cheng, L. Peng, M. Zu, Manipulating metals for adaptive thermal camouflage. *Sci. Adv.* **6**, eaba3494 (2020).
26. Y. Lee *et al.*, Mimicking human and biological skins for multifunctional skin electronics. *Adv. Funct. Mater.* **30**, 1904523 (2020).
27. Q. Wang, G. R. Gossweiler, S. L. Craig, X. Zhao, Cephalopod-inspired design of electro-mechano-chemically responsive elastomers for on-demand fluorescent patterning. *Nat. Commun.* **5**, 4899 (2014).
28. S. Ham *et al.*, One-dimensional organic artificial multi-synapses enabling electronic textile neural network for wearable neuromorphic applications. *Sci. Adv.* **6**, eaba1178 (2020).
29. D. G. Roe *et al.*, Biologically plausible artificial synaptic array: Replicating Ebbinghaus' memory curve with selective attention. *Adv. Mater.* **33**, e2007782 (2021).
30. Y. Kim *et al.*, A bioinspired flexible organic artificial afferent nerve. *Science* **360**, 998–1003 (2018).
31. H. Shim *et al.*, Fully rubbery synaptic transistors made out of all-organic materials for elastic neurological electronic skin. *Nano Res.* **15**, 758–764 (2022).
32. D.-G. Seo *et al.*, Versatile neuromorphic electronics by modulating synaptic decay of single organic synaptic transistor: From artificial neural networks to neuro-prosthetics. *Nano Energy* **65**, 104035 (2019).
33. L. Liu *et al.*, Stretchable neuromorphic transistor that combines multisensing and information processing for epidermal gesture recognition. *ACS Nano* **16**, 2282–2291 (2022).
34. D.-Y. Khang, H. Jiang, Y. Huang, J. A. Rogers, A stretchable form of single-crystal silicon for high-performance electronics on rubber substrates. *Science* **311**, 208–212 (2006).
35. D.-H. Kim *et al.*, Stretchable and foldable silicon integrated circuits. *Science* **320**, 507–511 (2008).
36. W. M. Choi *et al.*, Biaxially stretchable "wavy" silicon nanomembranes. *Nano Lett.* **7**, 1655–1663 (2007).
37. Y. Lim *et al.*, Biaxially stretchable, integrated array of high performance microsupercapacitors. *ACS Nano* **8**, 11639–11650 (2014).
38. J. A. Rogers, T. Someya, Y. Huang, Materials and mechanics for stretchable electronics. *Science* **327**, 1603–1607 (2010).
39. N. Matsuhisa *et al.*, Printable elastic conductors with a high conductivity for electronic textile applications. *Nat. Commun.* **6**, 7461 (2015).
40. Y.-S. Guan *et al.*, Air/water interfacial assembled rubbery semiconducting nanofilm for fully rubbery integrated electronics. *Sci. Adv.* **6**, eabb3656 (2020).
41. H. Shim *et al.*, Stretchable elastic synaptic transistors for neurologically integrated soft engineering systems. *Sci. Adv.* **5**, eaax4961 (2019).
42. H.-J. Kim, K. Sim, A. Thukral, C. Yu, Rubbery electronics and sensors from intrinsically stretchable elastomeric composites of semiconductors and conductors. *Sci. Adv.* **3**, e1701114 (2017).
43. C. S. Yang *et al.*, A synaptic transistor based on quasi-2D molybdenum oxide. *Adv. Mater.* **29**, 1700906 (2017).
44. X. Wang *et al.*, Stretchable synaptic transistors with tunable synaptic behavior. *Nano Energy* **75**, 104952 (2020).
45. H. J. Kim, A. Thukral, S. Sharma, C. Yu, Biaxially stretchable fully elastic transistors based on rubbery semiconductor nanocomposites. *Adv. Mater. Technol.* **3**, 1800043 (2018).
46. J. Zhu *et al.*, Ion gated synaptic transistors based on 2D van der Waals crystals with tunable diffusive dynamics. *Adv. Mater.* **30**, e1800195 (2018).
47. S. M. Kwon *et al.*, Environment-adaptable artificial visual perception behaviors using a light-adjustable optoelectronic neuromorphic device array. *Adv. Mater.* **31**, e1906433 (2019).
48. S. H. Park *et al.*, 3D printed polymer photodetectors. *Adv. Mater.* **30**, e1803980 (2018).
49. Y. Yang *et al.*, Long-term synaptic plasticity emulated in modified graphene oxide electrolyte gated IZO-based thin-film transistors. *ACS Appl. Mater. Interfaces* **8**, 30281–30286 (2016).
50. I. D. Rosca, S. V. Hoa, Highly conductive multiwall carbon nanotube and epoxy composites produced by three-roll milling. *Carbon* **47**, 1958–1968 (2009).
51. K. Sim *et al.*, Fully rubbery integrated electronics from high effective mobility intrinsically stretchable semiconductors. *Sci. Adv.* **5**, eaav5749 (2019).
52. J. Choi, R. Ghaffari, L. B. Baker, J. A. Rogers, Skin-interfaced systems for sweat collection and analytics. *Sci. Adv.* **4**, eaar3921 (2018).
53. A. Chortos, J. Liu, Z. Bao, Pursuing prosthetic electronic skin. *Nat. Mater.* **15**, 937–950 (2016).
54. C. K. Colton, Implantable biohybrid artificial organs. *Cell Transplant.* **4**, 415–436 (1995).
55. S. Raspopovic, Neurorobotics for neurorehabilitation. *Science* **373**, 634–635 (2021).
56. B. Mosadegh, H. Tavana, S. C. Lesher-Perez, S. Takayama, High-density fabrication of normally closed microfluidic valves by patterned deactivation of oxidized polydimethylsiloxane. *Lab Chip* **11**, 738–742 (2011).